

# WEIGHT SPACE REPRESENTATION LEARNING WITH NEURAL FIELDS

Zhuoqian Yang, Mathieu Salzmann, Sabine Süssstrunk

EPFL

<first>.<last>@epfl.ch

## ABSTRACT

In this work, we investigate the potential of weights to serve as effective representations, focusing on neural fields. Our key insight is that constraining the optimization space through a pre-trained base model and low-rank adaptation (LoRA) can induce structure in weight space. Across reconstruction, generation, and analysis tasks on 2D and 3D data, we find that multiplicative LoRA weights achieve high representation quality while exhibiting distinctiveness and semantic structure. When used with latent diffusion models, multiplicative LoRA weights enable higher-quality generation than existing weight-space methods.

## 1 INTRODUCTION

Neural network weights have traditionally been viewed as opaque byproducts of optimization, high-dimensional vectors that encode learned functions but resist interpretation or manipulation. This perspective has begun to shift with recent advances in weight space learning, where researchers have demonstrated that network parameters can be merged Yang et al. (2024); Singh et al.; Lim et al. (2024b), generated Erkoç et al. (2023); Peebles et al. (2023), or used as inputs to other networks Zhou et al. (2023b); Hospedales et al. (2020); Lim et al. (2024a). A fundamental question nonetheless remains largely unexplored: Can neural network weights themselves serve as meaningful representations for data?

We investigate this question in the context of implicit neural representations (INRs), where neural networks are trained to overfit individual samples by mapping coordinates to values. INRs have proven to be versatile, capable of encoding diverse data modalities within a unified architecture Xie et al. (2022). Since INRs inherently encode signals as network parameters, using these weights as representations is a natural next step. However, neural network weights are known to be ambiguous by nature, for example because neuron permutations and scaling leave the network function unchanged Zhao et al. (2025). As such, different random initializations may yield vastly different parameter configurations yet functionally identical models. In other words, functionally identical networks can be arbitrarily far in weight space Zhao et al. (2025), challenging the use of network weights as data representations.

Our key insight is that constraining the network weights of different samples by introducing appropriate inductive biases allows us to transform these chaotic parameters into organized, semantic representations. To this end, as illustrated in Figure 1, we propose to use Low-Rank Adaptation (LoRA) Hu et al. (2022) within a pre-trained base neural field to create structured weight space representations. This design is motivated by two key properties of LoRA: First, adaptation through LoRA constrains the weight updates to lie within a low-dimensional subspace defined by the base model. Hu et al. Hu et al. (2022) demonstrate this through subspace similarity analysis, showing that adaptations at different ranks share common singular vector directions, suggesting the existence of a meaningful low-rank adaptation subspace. Second, the low-rank constraint inherently reduces the dimensionality of the weight space representation, mitigating the curse of dimensionality that would otherwise hinder learning in high-dimensional parameter spaces.

Notably, we find that the standard additive LoRA formulation is insufficient for weight space learning in the context of neural fields. Instead, we introduce multiplicative LoRA (mLoRA),

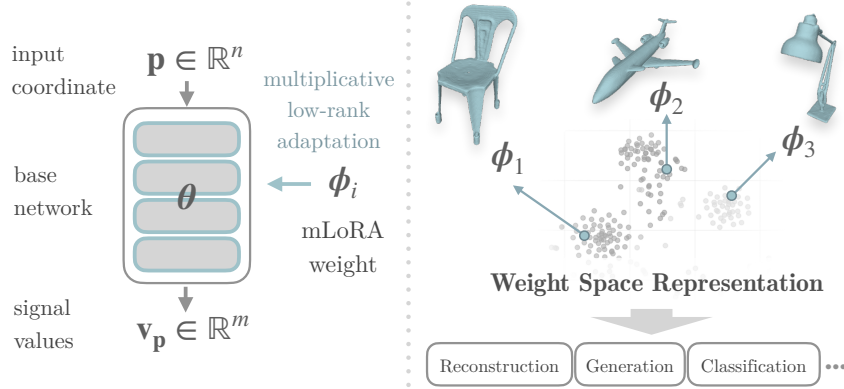


Figure 1: LoRA based weight space representation with neural fields. Given an input coordinate  $\mathbf{p} \in \mathbb{R}^n$ , a base neural field is adapted via multiplicative LoRA weights  $\phi_i$  to produce signal values  $\mathbf{v}_{\mathbf{p}} \in \mathbb{R}^m$ , each weight representing an instance. The LoRA weights themselves form structured representations in weight space, enabling diverse applications including reconstruction, generation, and clustering.

where weight updates are applied through element-wise multiplication rather than addition. This multiplicative formulation naturally aligns with modulation mechanisms in generative neural fields Anokhin et al. (2021); Karras et al. (2021); Chan et al. (2020), where features are composed through multiplicative interactions, enabling effective weight space learning.

We validate our approach across multiple data modalities and tasks. First, we establish that LoRA-based weight representations achieve lower reconstruction error, greater robustness to initialization, and better linear mode connectivity than vanilla INR weights. Second, we demonstrate that these structured weight spaces support high-quality generative modeling, with diffusion models trained on multiplicative LoRA weights outperforming prior attempts in weight space neural field generation. Finally, through evaluation on discriminative tasks (*i.e.* classification and clustering), we confirm that the weight space structure correlates with semantic properties of the encoded data.

Our contributions can be summarized as follows:

1. We demonstrate that neural network weights, when properly constrained, can serve as effective data representations that capture semantic structure.
2. We introduce multiplicative LoRA for neural fields, which we show provides superior representation quality compared to standard additive LoRA and vanilla weight parameterizations.
3. We validate weight space representations across diverse tasks: Reconstruction, generation, and analysis, establishing their viability as a representation paradigm.

## 2 RELATED WORK

### 2.1 WEIGHT SPACE LEARNING

The treatment of neural network weights as learnable representations has emerged as a distinct research direction, progressing from early hypernetwork approaches to sophisticated weight-space generative models. Early work demonstrated that network parameters could be generated by auxiliary networks Ha et al. (2016), though these methods suffered from prohibitive memory overhead when scaling to modern architectures Wang & Others (2025). The fundamental challenge of weight space manipulation stems from permutation symmetry: Functionally identical networks can have vastly different parameter configurations due to neuron reordering Gao & Others (2024); Navon et al. (2023).

Recent advances have addressed these challenges through multiple strategies. Model merging techniques leverage optimal transport and activation matching to align neurons before parameter fusion Singh & Jaggi (2020); Ormaniec & Others (2025), while equivariant architectures explicitly respect weight-space symmetries when processing network parameters Navon et al. (2023); Kofinas et al. (2024). A parallel research direction focuses on building neural networks that process weights as inputs. Neural Functional Transformers Zhou et al. (2023b) and permutation-equivariant neural functionals Zhou et al. (2023a) construct architectures that can extract information from network parameters while respecting their symmetries. Methods operating on Low-Rank Adaptation (LoRA) weights Lim et al. (2024a) develop GL-equivariant networks to process low-rank weight spaces of fine-tuned models.

Our work differs fundamentally from these weight-processing approaches: Rather than building encoders or networks that consume weights as inputs, we investigate whether optimization-derived weights can *directly* serve as representations without additional encoding steps. This distinction positions our contribution as exploring the intrinsic representational quality of weight spaces rather than developing architectures for weight-space processing.

Generative modeling in weight space has seen significant progress, with diffusion models now capable of synthesizing functional neural networks. Weight-space generation with diffusion models Wang et al. (2024); Wang & Others (2025); Peebles et al. (2023) has been explored for generating models for image classification. With a different focus, our work explore neural neural field weights as representation of data that support high-quality generation and encode semantic structure.

## 2.2 IMPLICIT NEURAL REPRESENTATIONS

Implicit Neural Representations (INRs), also known as neural fields, are continuous functions parameterized by neural networks that map coordinates to signal values. INRs represent signals as continuous functions  $\Phi : \mathbb{R}^n \rightarrow \mathbb{R}^m$ , where a neural network maps  $n$ -dimensional coordinates to  $m$ -dimensional quantities. This paradigm enables resolution-independent, memory-efficient representations of complex signals.

The versatility of INRs has been extensively documented Xie et al. (2022); Essakine et al. (2024). These representations are fundamentally data-agnostic, employing identical network architectures across diverse modalities including 1D audio, 2D images, 3D shapes, and even 4D spatiotemporal data.

Beyond single-instance fitting, generalizable INRs have been proposed to learn priors across datasets through approaches based on autoencoders Park et al. (2019), generative adversarial networks (GANs) Anokhin et al. (2021); Karras et al. (2021); Chan et al. (2020) and shared layers Vyas et al. (2024). The GAN-based works could be seen as extensions of the StyleGAN Karras et al. (2019) paradigm into the realm of neural fields. They generate different instances by modulating an MLP trunk, upon which we build as base network.

Because INRs parameterize data as neural network functions, the weights offer a direct pathway to data representation. This perspective has practical applications in compression, with methods Dupont et al. (2021); Gordon et al. (2024) demonstrating competitive compression ratios by storing quantized network parameters instead of raw data. However, whether the collection of weights could encode semantic structure remains an open question. Another line of work employs hypernetworks Kloeck et al. (2019) and transformers Chen & Wang (2022) to predict INR weights from input data via learned mappings as way of data generation. In contrast, we investigate whether gradient-descent-optimized weights can directly serve as meaningful representations. HyperDiffusion Erkoç et al. (2023) train a diffusion transformer to generate neural field weights as mean of synthesizing 3D shapes and 4D animated shapes. Our work build on this work to further explore what ensures successful weight space generative modeling as well as explore semantic structures in neural field weights.

### 3 METHOD

We begin by establishing weight space representations via Low-Rank Adaptation of pre-trained base neural fields (Section 3.1). We then introduce multiplicative LoRA, a key modification that enables effective weight space learning for neural fields (Section 3.2). Next, we describe the base model architecture and training procedure (Section 3.3), followed by asymmetric masking to address permutation symmetry (Section 3.4). Finally, we present a hierarchical diffusion transformer for generative modeling in weight space (Section 3.5).

#### 3.1 WEIGHT SPACE REPRESENTATION

Given a dataset consisting of a collection of instances  $\{\mathbf{x}_i\}_{i=1}^N$ , we optimize one neural field for each instance. Each instance is then represented by the weights of its corresponding network, forming a weight space representation.

The simplest way to represent an instance with network weights consists of using standalone MLP weights. For each instance  $\mathbf{x}_i$ , we fit a small MLP from scratch. The instance  $\mathbf{x}_i$  is then represented with the weights of the MLP  $\boldsymbol{\theta}_i$ . Formally,

$$\boldsymbol{\theta}_i = \min_{\boldsymbol{\theta}} \mathcal{L}_{\text{recon}} [f(\mathbf{p} \mid \boldsymbol{\theta}), \mathbf{x}_i(\mathbf{p})] , \quad (1)$$

where  $\mathbf{p}$  is a spatial coordinate. The architecture consists of a Fourier Feature layer followed by two linear layers. We evaluate this approach as a baseline, to encourage consistency, all MLPs share the same random initialization across different instances as is done in Erkoç et al. (2023).

Encouraged by the observation that LoRA weights converge to a certain subspace Hu et al. (2022), which indicates that the base network enforce a certain structure on the space of LoRA weights, we fine tune a pre-trained base model using Low-Rank Adaptation (LoRA). For each instance  $\mathbf{x}_i$ , we optimize LoRA parameters  $\boldsymbol{\phi}_i = \{\mathbf{A}_i^l, \mathbf{B}_i^l\}_{l=1}^L$  across  $L$  layers while keeping the base weights frozen. That is, we solve

$$\boldsymbol{\phi}_i = \min_{\boldsymbol{\phi}} \mathcal{L}_{\text{recon}} [f(\mathbf{p} \mid \text{LoRA}(\mathbf{W}, \boldsymbol{\phi})), \mathbf{x}_i(\mathbf{p})] , \quad (2)$$

where  $\mathbf{W}$  denotes the frozen base model weights and  $\mathcal{L}_{\text{recon}}$  is a reconstruction loss. The instance  $\mathbf{x}_i$  is then represented with the LoRA weights  $\boldsymbol{\phi}_i$ , illustrated in Figure 1. Like is done for Standalone MLP weights, all LoRA share the same initialization.

#### 3.2 MULTIPLICATIVE LoRA

We employ multiplicative LoRA rather than the standard additive formulation. Standard LoRA Hu et al. (2022) adapts a pre-trained weight matrix  $\mathbf{W} \in \mathbb{R}^{d_{\text{out}} \times d_{\text{in}}}$  through additive low-rank updates  $\mathbf{W}' = \mathbf{W} + \mathbf{B}\mathbf{A}$  where  $\mathbf{A} \in \mathbb{R}^{r \times d_{\text{in}}}$  and  $\mathbf{B} \in \mathbb{R}^{d_{\text{out}} \times r}$  are low-rank matrices with rank  $r \ll \min(d_{\text{in}}, d_{\text{out}})$ . We introduce a multiplicative formulation that applies weight updates through elementwise multiplication as

$$\mathbf{W}' = \mathbf{W} \odot \mathbf{B}\mathbf{A} , \quad (3)$$

where  $\odot$  denotes elementwise multiplication. This formulation enables more effective modulation of features, analogous to successful modulation techniques in generative neural fields Anokhin et al. (2021); Karras et al. (2021); Chan et al. (2020). In our experiments, we demonstrate that this design is a critical to obtaining good weight space structure and performance on reconstruction, generation and discriminative tasks.

#### 3.3 BASE MODEL ARCHITECTURE AND TRAINING

For LoRA-based representations, we require a strong base model that captures transferable features across the data distribution. We adopt a coordinate-based neural field architecture with multiplicative weight modulation, a design found across multiple generative neural field works Anokhin et al. (2021); Karras et al. (2021); Chan et al. (2020). The network consists of an MLP-based trunk, where variations across instances are injected through multiplicative



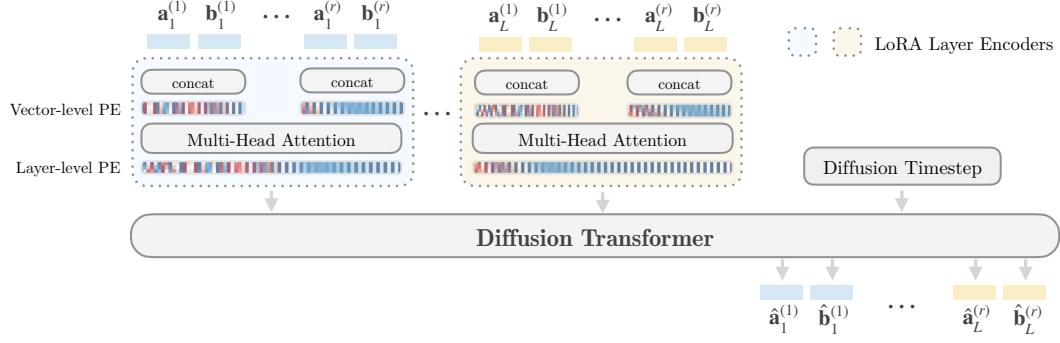


Figure 2: **Diffusion Transformer with hierarchical LoRA layer encoder architecture.** For each layer  $l$ , we treat vector pairs  $(\mathbf{a}_l^{(i)}, \mathbf{b}_l^{(i)})$  as tokens. Vector-level positional encodings capture rank dimension indices, followed by multi-head attention that models interactions among the  $r$  rank components within the layer. This hierarchical design enables the model to learn both local (within-layer) dependencies among rank components and global (cross-layer) relationships across different layers of the neural field.

weight modulation. This modulation mechanism naturally aligns with our multiplicative LoRA formulation, and the architecture is applicable, but not limited, to 2D and 3D data.

We train the base model using the variational autoencoder paradigm Park et al. (2019). This training scheme is desirable because it requires no encoder design, aligning with the data-agnostic quality of INRs. Given a dataset  $\{\mathbf{x}_i\}_{i=1}^N$ , we jointly optimize the network parameters  $\theta$  and per-instance latent codes  $\{\mathbf{z}_i\}_{i=1}^N$  by solving

$$\min_{\theta, \{\mathbf{z}_i\}} \sum_{i=1}^N \mathcal{L}_{\text{recon}}(f_{\theta}(\mathbf{p}, \mathbf{z}_i), \mathbf{x}_i(\mathbf{p})) + \lambda_r \|\mathbf{z}_i\|_2^2, \quad (4)$$

where  $\mathbf{p}$  represents spatial coordinates and  $\lambda_r$  controls the latent code regularization.

### 3.4 ASYMMETRIC MASK FOR PERMUTATION SYMMETRY

Permutation symmetry refers to the invariance of network functions under neuron reordering, which causes functionally identical networks to occupy vastly different locations in weight space Zhao et al. (2025); Gao & Others (2024); Navon et al. (2023). Although LoRA weights converge to a certain subspace Hu et al. (2022), permutation symmetry remains present even within LoRA parameterizations, affecting both additive and multiplicative formulations. In additive LoRA, the operation  $\mathbf{BA}$  can be viewed as a two layer network:  $\mathbf{A}$  acts as an encoder compressing to  $r$  hidden activations, and  $\mathbf{B}$  acts as a decoder expanding back. Permuting these  $r$  hidden dimensions preserves the function, inducing an  $r!$ -fold symmetry. In multiplicative LoRA, the adapted weight matrix decomposes into a sum of terms, each being the base weight matrix scaled by diagonal matrices. Permuting the rank dimensions in this sum preserves the output due to commutative addition, again leading to permutation symmetry. We provide formal proofs for both cases in the appendix. Notably, multiplicative LoRA weights are aligned with base network channels once permutation symmetry is eliminated, see Corollary 2.2.

To address this symmetry, we investigate the asymmetric masking technique of Lim et al. (2024b), designed to eliminate permutation symmetry during optimization. For each layer, we randomly freeze  $\sqrt{d_{\text{out}}}$  entries in each row of the weight matrix, where  $d_{\text{out}}$  is the out dimension. The frozen entries and their positions are shared across different runs. The values of the frozen entries are determined as follows. Suppose entry  $\mathbf{W}_{ij}$  is chosen to be fixed. For the standalone MLP and additive LoRA, we initialize the frozen entries with higher variance:  $\mathbf{W}_{ij} \sim \mathcal{N}(0, \kappa \mathbf{I})$ . with the other weights being initialized with  $\mathcal{N}(0, \mathbf{I})$ . In the case of multiplicative LoRA, we simply zero out the frozen entries:  $\mathbf{W}_{ij} \leftarrow 0$ . This is natural for the multiplicative formulation.

While asymmetric masking was originally developed for standalone MLPs and can be applied to all three parameterizations, it proves most effective for multiplicative LoRA in the neural field domain. For standalone MLPs and additive LoRA, the technique requires large variance  $\kappa$  for the frozen entries to break symmetry effectively Lim et al. (2024b). However, this is problematic for neural fields, which synthesize signals through additive composition. In this regime, fixing certain weights to large magnitudes creates entanglement: other weights must compensate by canceling out these fixed signals, leading to difficult optimization landscapes. Multiplicative LoRA avoids this issue by zeroing out frozen entries, effectively removing certain signal components rather than forcing compensation. This approach aligns naturally with the multiplicative structure and avoids weight entanglement. We validate this advantage empirically in our experiments.

### 3.5 DIFFUSION MODEL ON WEIGHT REPRESENTATIONS

To evaluate the potential of the weight representations in generative tasks, we train diffusion models to learn their distribution. Following the DDPM framework, we define a forward diffusion process that gradually adds Gaussian noise to the weight representations, i.e.

$$q(\phi_t|\phi_{t-1}) = \mathcal{N}(\phi_t; \sqrt{1 - \beta_t}\phi_{t-1}, \beta_t\mathbf{I}) , \quad (5)$$

where  $\phi$  represents the flattened weight parameters (either full MLP weights or LoRA matrices), and  $\beta_t$  follows a linear schedule from  $10^{-4}$  to  $2 \times 10^{-2}$  over  $T$  timesteps.

We parameterize the reverse process using a diffusion transformer (DiT) Peebles & Xie (2022) that predicts the noise added to the weights. For standalone MLP weights, we adopt the architecture from Erkoç et al. (2023); Peebles et al. (2023). For LoRA weights, we design a hierarchical LoRA layer encoder module that respects the structural properties of low-rank weight matrices, shown in Figure 2. Each layer  $l$  is processed as follows. First, we treat each vector pair  $(\mathbf{a}_l^{(i)}, \mathbf{b}_l^{(i)})$  as a token, where  $\mathbf{a}_l^{(i)}$  and  $\mathbf{b}_l^{(i)}$  are the  $i$ -th columns and rows of matrices  $\mathbf{A}^{(l)}$  and  $\mathbf{B}^{(l)}$ , respectively. Vector-level positional encodings are then applied to capture the rank dimension index. A multi-head attention module with  $r$  attention heads encodes the interactions among the  $r$  vector pairs within the layer, allowing the model to learn dependencies between different rank components. Finally, layer-level positional encodings are applied to the aggregated layer representation before feeding into the main transformer.

This hierarchical design is motivated by the compositional structure of LoRA weights. Within each layer, the low-rank decomposition creates dependencies among the  $r$  rank components, which the intra-layer attention module explicitly models. Different layers, however, operate at different semantic levels in the neural field, making layer-level encoding essential for capturing cross-layer relationships. This architecture naturally respects the paired nature of LoRA matrices while enabling the model to learn both local (within-layer) and global (cross-layer) weight space structure.

With the noise prediction network  $\epsilon_\theta(\phi_t, t)$ , we optimize the simplified diffusion objective

$$\mathcal{L} = \mathbb{E}_{t \sim \mathcal{U}(1, T), \phi_0 \sim p_{\text{data}}, \epsilon \sim \mathcal{N}(0, \mathbf{I})} [\|\epsilon - \epsilon_\nu(\phi_t, t)\|^2] . \quad (6)$$

During inference, we use DDIM sampling to generate new weight representations, which are then used to instantiate novel neural fields.

## 4 EXPERIMENTS

We conduct experiments to inspect the structure of the weight space and evaluate weight space representations across reconstruction, generation, and discriminative tasks.

**Datasets.** We evaluate on two datasets. For 2D data, we use FFHQ Karras et al. (2019), which contains high quality face images. We evaluate at the resolution of  $128 \times 128$ , although modest compared to current state-of-the-art in image generation, this resolution is significantly higher than what previous weight-space methods Zhou et al. (2023b;a) have evaluated on and therefore more challenging. For 3D data, we use ShapeNet Chang et al.

Table 1: Reconstruction quality. We report the PSNR for 2D FFHQ, the Chamfer Distance  $\times 10^{-2}$  for 3D ShapeNet, and the number of trainable parameters in each weight space representation. Parameters frozen by the asymmetric mask are reduced from the count.

	FFHQ		ShapeNet		
	PSNR $\uparrow$	# Params	CD-A $\downarrow$	CD-M $\downarrow$	# Params
MLP	35.11	27,357	2.57	3.78	30,196
MLP-Asym	33.28	24,537	2.64	4.00	27,226
LoRA	35.69	27,395	2.44	3.39	29,696
LoRA-Asym	24.63	26,307	2.46	3.44	27,539
mLoRA	35.65	27,395	2.45	3.49	29,696
mLoRA-Asym	<b>36.91</b>	26,307	<b>2.41</b>	<b>3.35</b>	27,539

(2015), focusing on two settings: A single-category model trained on airplanes, and a multi-category model trained on ten object categories including airplanes, chairs, tables, and other common objects.

**Candidate Representations.** We compare six weight space representations: (1) *MLP*: standalone MLP weights; (2) *MLP-Asym*: standalone MLP weights with asymmetric masking; (3) *LoRA*: additive LoRA weights; (4) *LoRA-Asym*: additive LoRA weights with asymmetric masking; (5) *mLoRA*: multiplicative LoRA weights; and (6) *mLoRA-Asym*: multiplicative LoRA weights with asymmetric masking. This design allows us to isolate the effects of parameterization (standalone vs LoRA), operation type (additive vs multiplicative), and symmetry breaking (with or without asymmetric masks).

#### 4.1 RECONSTRUCTION

The reconstruction task directly corresponds to the fitting procedure described in Section 3.1, where each weight space representation is optimized to reconstruct individual instances. For 2D images, we measure the PSNR (higher is better). For 3D shapes, we measure the Chamfer Distance (lower is better). We also report the number of learnable parameters for each representation.

**Results.** As shown in Table 1, LoRA, mLoRA and mLoRA-Asym achieve better reconstruction quality while maintaining a compact parameter count, compared to the MLP-based weight representations. We attribute this to the inductive bias provided by the base network, which captures transferable features across instances, and fine tuning effectively leverages these shared representations with minimal adaptation parameters. Multiplicative LoRA perform better than its additive counterpart, echoing the wide application of multiplicative modulation in generative neural fields Anokhin et al. (2021); Chan et al. (2020); Karras et al. (2021). Surprisingly, mLoRA-Asym consistently outperforms mLoRA despite having certain parameters frozen by the asymmetric mask. Our hypothesis is that the masking further reduces parameter entanglement and thereby improves the reconstruction accuracy. Also notably, LoRA-Asym performs poorly on FFHQ, likely due to increased parameter entanglement caused by large variance  $\kappa = 6$  (empirically determined) of the frozen weights, as discussed in Section 3.4.

#### 4.2 WEIGHT SPACE STRUCTURE ANALYSIS

To understand the geometric properties of different weight spaces, we conduct a stability analysis on the ShapeNet airplane model. This experiment examines whether different random initializations lead to similar weight configurations after optimization. We independently optimize two models for each instance, starting from different initialization points. The first model is initialized with  $\boldsymbol{\iota}_1 \sim \mathcal{N}(0, \mathbf{I})$ , while the second is initialized with a (variance preserving) perturbed code  $\sqrt{1 - \lambda^2} \boldsymbol{\iota}_1 + \lambda \boldsymbol{\iota}_2$  where  $\boldsymbol{\iota}_2 \sim \mathcal{N}(0, \mathbf{I})$  and  $\lambda$  controls the

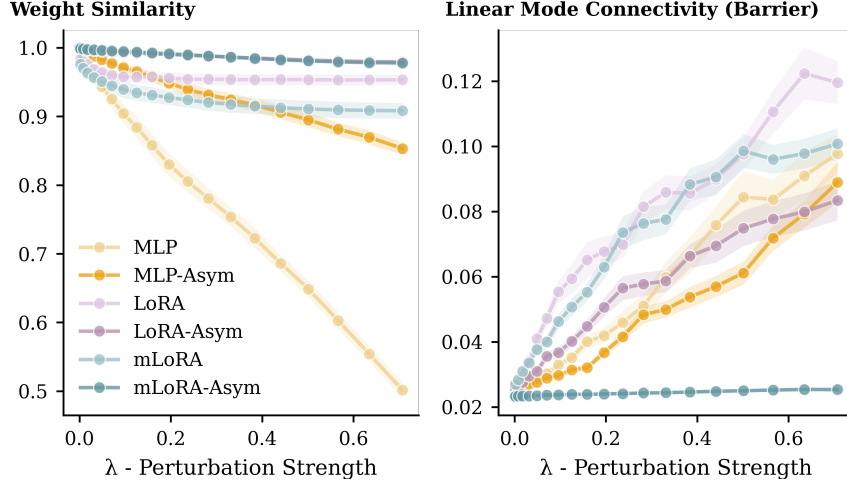


Figure 3: **Weight space structure analysis.** We measure weight similarity (cosine similarity) and the linear mode connectivity barrier (Chamfer distance) as a function of initialization perturbation strength  $\lambda$ . Each data point is averaged from 30 instances, the underlying shades are indicative of standard deviation.

perturbation strength. The optimized weights from these two runs are obtained as

$$\begin{aligned}\phi &= \arg \min_{\phi'} \mathcal{L}_{\text{recon}} [f_{\phi'}(\cdot | \mathbf{t}_1), \mathbf{x}] , \\ \phi_{\lambda} &= \arg \min_{\phi'} \mathcal{L}_{\text{recon}} \left[ f_{\phi'} \left( \cdot | \sqrt{1 - \lambda^2} \mathbf{t}_1 + \lambda \mathbf{t}_2 \right), \mathbf{x} \right] ,\end{aligned}$$

where  $\mathbf{x}$  denotes the target instance. We evaluate two metrics to assess weight space structure. First, we measure weight similarity using the cosine similarity: A high cosine similarity indicates that different optimization paths converge to similar weight configurations.

Second, to examine linear mode connectivity Frankle et al. (2020), we measure the barrier height by evaluating reconstruction quality at the midpoint of the linear interpolation path. Specifically, we compute the Chamfer Distance between the ground truth mesh vertices  $\mathbf{v}_{\text{gt}}$  and the vertices  $\mathbf{v}_{\text{avg}}$  extracted via marching cubes from the averaged weights, i.e.,

$$b(\phi, \phi_{\lambda}) = \text{CD} \left( \mathbf{v}_{\text{gt}}, \mathcal{M} \left( f_{\frac{\phi + \phi_{\lambda}}{2}} \right) \right) ,$$

where  $\mathcal{M}(\cdot)$  denotes the marching cubes algorithm and  $\text{CD}(\cdot, \cdot)$  denotes the Chamfer Distance. Figure 3 presents the results across varying perturbation strengths  $\lambda$  for the six candidate representations.

**Results.** Figure 3 reveals that LoRA and mLoRA improve weight similarity compared to standalone MLPs. Specifically, weight similarity for MLP and MLP-Asym decreases approximately linearly with perturbation strength, while LoRA-based representations exhibit a saturation trend at large perturbation strengths. However, it appears that applying LoRA does not improve linear mode connectivity. This is not unexpected since permutation symmetry still exist in LoRA weights, as discussed in Section. 3.4.

Although not always improving reconstruction quality, the asymmetric mask improves both weight similarity and linear mode connectivity across all parameterizations. Notably, mLoRA-Asym exhibits exceptional behavior: weight similarity remains very high and the barrier remains very low even with very different initializations. This suggests that mLoRA-Asym weights **converge to a linear mode**. The reason is likely that multiplicative LoRA weights are aligned with base networks, once permutation symmetry is eliminated, as we prove in Corollary 2.2 in the Appendix.

Despite the application of the asymmetric mask, additive LoRA weights does not exhibit good linear mode connectivity as mLoRA does. We hypothesize this is related to the internal

Table 2: Weight space generation performance on 2D FFHQ.

	FD ↓	MMD-G ↓	MMD-P ↓
HyperDiffusion	0.241	0.158	1.887
MLP-Asym	0.287	0.203	2.423
LoRA	0.321	0.169	2.018
LoRA-Asym	0.269	0.157	1.877
mLoRA	0.100	0.056	0.674
mLoRA-Asym	<b>0.073</b>	<b>0.039</b>	<b>0.467</b>

Table 3: Weight space generation performance on 3D ShapeNet. We examine a model trained on a single category *Airplane* and a 10-category model *Multi*.

	mMD ↓	COV ↑	1-NNA ↓	FD ↓	MMD-G ↓	MMD-P ↓
<b>ShapeNet - Airplane</b>						
HyperDiffusion	2.39	43.6%	78.2%	0.027	0.009	0.122
MLP-Asym	2.80	44.8%	80.9%	0.041	0.018	0.254
LoRA	116.4	3.1%	99.9%	1.553	0.669	7.163
LoRA-Asym	270.6	2.0%	100%	1.532	0.823	7.931
mLoRA	1.96	<b>46.2%</b>	<b>70.5%</b>	0.049	0.025	0.359
mLoRA-Asym	<b>1.89</b>	43.4%	71.9%	<b>0.011</b>	<b>0.003</b>	<b>0.041</b>
<b>ShapeNet - Multi</b>						
HyperDiffusion	8.64	41.6%	78.3%	0.117	0.023	0.219
MLP-Asym	7.77	46.5%	74.0%	0.085	0.016	0.157
LoRA	152.9	10.9%	99.1%	1.014	0.319	2.501
LoRA-Asym	210.0	1.2%	100%	1.241	0.437	2.987
mLoRA	5.75	46.4%	61.9%	0.071	0.011	0.123
mLoRA-Asym	<b>5.52</b>	<b>49.6%</b>	<b>58.6%</b>	<b>0.026</b>	<b>0.004</b>	<b>0.040</b>

mechanisms of neural fields. Neural fields synthesize signals through iterative composition: linear layers combine basic signal components, while activation functions generate harmonics Yüce et al. (2022). When neural fields are optimized on individual instances, their channels become highly entangled. However, when trained on multiple instances in a generalizable setting, the network learns transferable features and exhibits greater disentanglement Radford et al. (2021). This observation provides additional motivation for fine-tuning a base network trained in the generative regime. Additive LoRA reintroduces entanglement by mixing features across channels, whereas multiplicative LoRA preserves the channel structure through aligned feature scaling, avoiding additional entanglement.

### 4.3 GENERATION VIA DIFFUSION MODELS

We evaluate the generative capabilities of different weight space representations by training diffusion models on each parameterization. This experiment tests whether the learned weight spaces support high-quality generative modeling.

**Implementation.** For standalone MLP weights, we use the same diffusion model architecture as HyperDiffusion Erkoç et al. (2023). For LoRA weights, we employ our hierarchical LoRA layer encoder described in Section 3.5. For standalone MLP weights and standalone MLP weights with asymmetric masks, we adopt the initialization technique from Erkoç et al. (2023), which first fits one instance and then uses its weights to initialize all other fittings. This can be viewed as fine tuning a small MLP fitted to one instance to other instances, enabling direct comparison with the state-of-the-art weight space diffusion method.

**Evaluation Metrics.** For both 2D and 3D data, we measure the difference between the distribution of the generated and reference samples. We compute the Fréchet distance

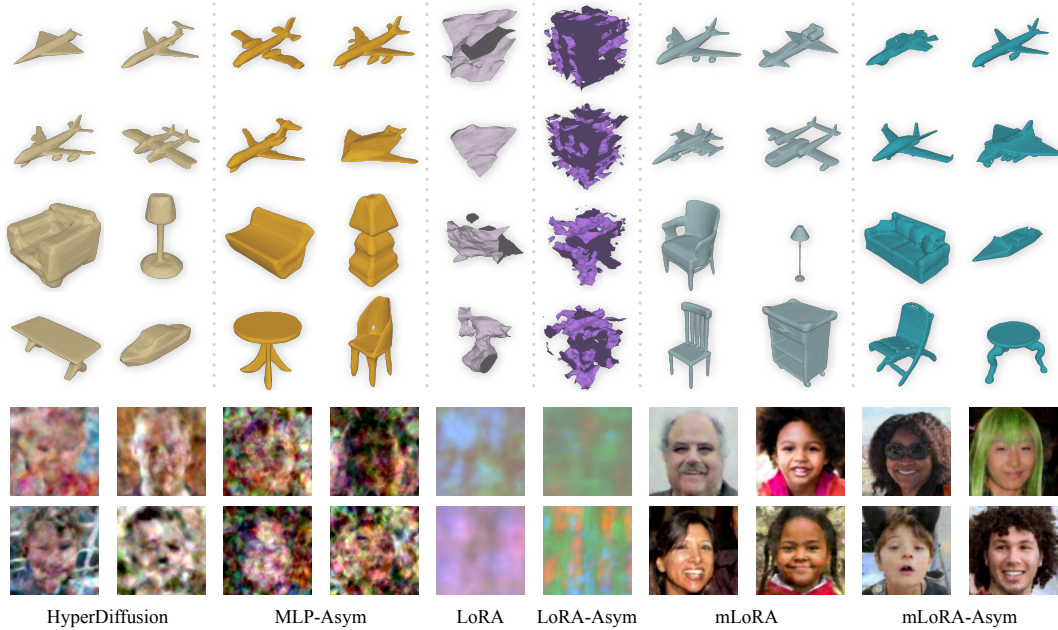


Figure 4: **Qualitative generation results.** Generated samples from diffusion models trained on different weight space representations. The top 2 rows show results generated by the *Airplane* model, followed by 2 rows from the *Multi-class* model. The bottom rows show 2D FFHQ generations.

(FD) Fréchet (1957), as well as the Maximum Mean Discrepancy (MMD) calculated using a Gaussian RBF kernel (MMD-G) and a polynomial kernel (MMD-P), which has been shown to be more reliable and sample efficient than the Fréchet distance Heusel et al. (2017); Bińkowski et al. (2018). These metrics operate on features extracted by deep learned models, as deep learned feature extractors project the data into semantically rich embedding spaces where distances better correlate with human perception of similarity. We employ these metrics in their mathematical form rather than using modality-specific implementations like FID Heusel et al. (2017) or KID Bińkowski et al. (2018), as this allows for consistent evaluation across different data modalities. For 2D images, we use CLIP Radford et al. (2021) as the feature extractor; for 3D shapes, we use a PointNet++ Qi et al. (2017). For 3D shapes, following Erkoç et al. (2023); Vahdat et al. (2022); Luo & Hu (2021); Zhou et al. (2021), we also report distance-based metrics: Minimum Matching Distance (mMD), Coverage (COV), and 1 Nearest Neighbor Accuracy (1-NNA). These metrics use the Chamfer Distance to measure shape similarity. Formal definitions are presented in the supplementary material.

**Results.** Quantitative results are reported in Table 2 for 2D FFHQ and Table 3 for 3D ShapeNet airplane, and ShapeNet ten category datasets. Figure 4 shows visual comparisons of generated samples. The quantitative results reveal several noteworthy patterns. First, mLoRA-Asym achieves the best performance across nearly all metrics on both 2D and 3D data, capable of generating diverse samples and capturing high-frequency details. This superior generative capability correlates directly with its favorable weight space structure, suggesting that weight space geometry is crucial for effective diffusion based generation. On ShapeNet, HyperDiffusion demonstrates competent performance on the single category airplane model, but degrades substantially on the multi category setting. This suggests difficulty in modeling a diverse weight distribution spanning multiple object classes. On FFHQ, HyperDiffusion fails to produce recognizable face images, whereas both mLoRA and mLoRA-Asym manage. This represents the first successful weight space generation for high resolution natural image generation. Previous methods have been restricted to simpler datasets such as MNIST and CIFAR. In contrast, LoRA and LoRA-Asym fail across all settings. We hypothesize that this relates to their poor weight space structure caused by entanglement of additive weights, as discuss in our weight space structure analysis. Overall,

Table 4: Classification and clustering results on the ShapeNet ten-category dataset. We report the accuracy for two classification methods and the Adjusted Rand Score for clustering. All results are statistics from 10 runs with random data split and initializations.

	Clustering ARI $\uparrow$	1-NN $\uparrow$	Logistic $\uparrow$
MLP	39.3% $\pm$ 3.1%	50.0% $\pm$ 3.0%	78.1% $\pm$ 1.3%
MLP-Asym	48.4% $\pm$ 3.7%	46.8% $\pm$ 4.2%	82.1% $\pm$ 1.2%
LoRA	56.3% $\pm$ 3.3%	75.2% $\pm$ 1.7%	86.1% $\pm$ 1.1%
LoRA-Asym	47.4% $\pm$ 4.4%	59.1% $\pm$ 10.4%	84.3% $\pm$ 0.8%
mLoRA	<b>67.1%</b> $\pm$ 3.7%	<b>85.1%</b> $\pm$ 1.8%	<b>90.0%</b> $\pm$ 0.7%
mLoRA-Asym	56.5% $\pm$ 2.7%	80.8% $\pm$ 1.6%	84.5% $\pm$ 1.4%

the strong correlation between weight space structure and generation performance validates that structured, well behaved weight spaces are essential for treating network parameters as effective data representations.

#### 4.4 DISCRIMINATIVE TASKS

To evaluate the distinctiveness and semantic structure of the learned weight representations, we conduct classification and clustering experiments on the ShapeNet ten-category dataset.

**Classification.** We evaluate two classification approaches. First, we use first nearest neighbor classification, which assigns each test weight to the category of its nearest neighbor in the training set using cosine similarity. Second, we train a linear classifier using logistic regression. All classifiers take the flattened weight representations as input and predict object categories.

**Clustering.** For clustering, we apply  $k$ -means with  $k = 10$  (matching the number of categories) on the weight representations. We evaluate the clustering quality using the Adjusted Rand Index (ARI), which measures the agreement between the predicted clusters and the ground-truth categories while correcting for chance.

**Results.** Table 4 reports the accuracy for the two classification methods and the Adjusted Rand Score for clustering across the six candidate representations. We also present t-SNE visualizations of the weight representations for the ten object categories in Figure 5. Each point encodes one instance, colored by its category. The classification and clustering results reveal a clear progression in semantic structure across different parameterizations. LoRA outperforms standalone MLPs, mLoRA outperforms LoRA, and mLoRA delivers the best results overall, achieving 90% accuracy with a linear classifier. Given that mLoRA-Asym exhibits better weight space structure in terms of linear mode connectivity, this result indicates that the discriminative power of the weight representation is not directly linked to linear mode connectivity or permutation symmetry. The t-SNE visualizations show that all weight representations are able to capture some level of semantic structure, as same-category instances are positioned closely. However, only multiplicative LoRA weights demonstrate clear class separation. These results substantiate that multiplicative LoRA weight representations are capable of capturing semantic structure. Notably, recent work *weights2weights* Dravid et al. (2024) similarly observes that LoRA weights that fine-tune image diffusion model exhibit interpretable structure with semantic linear directions, echoing our observations in the context of neural fields. Our finding further challenges the popular view that neural network weights are uninterpretable, demonstrating that with appropriate parameterization, weight spaces can encode semantic information.

## 5 LIMITATION

While our work establishes that neural network weights can serve as effective data representations, several limitations present opportunities for future research.

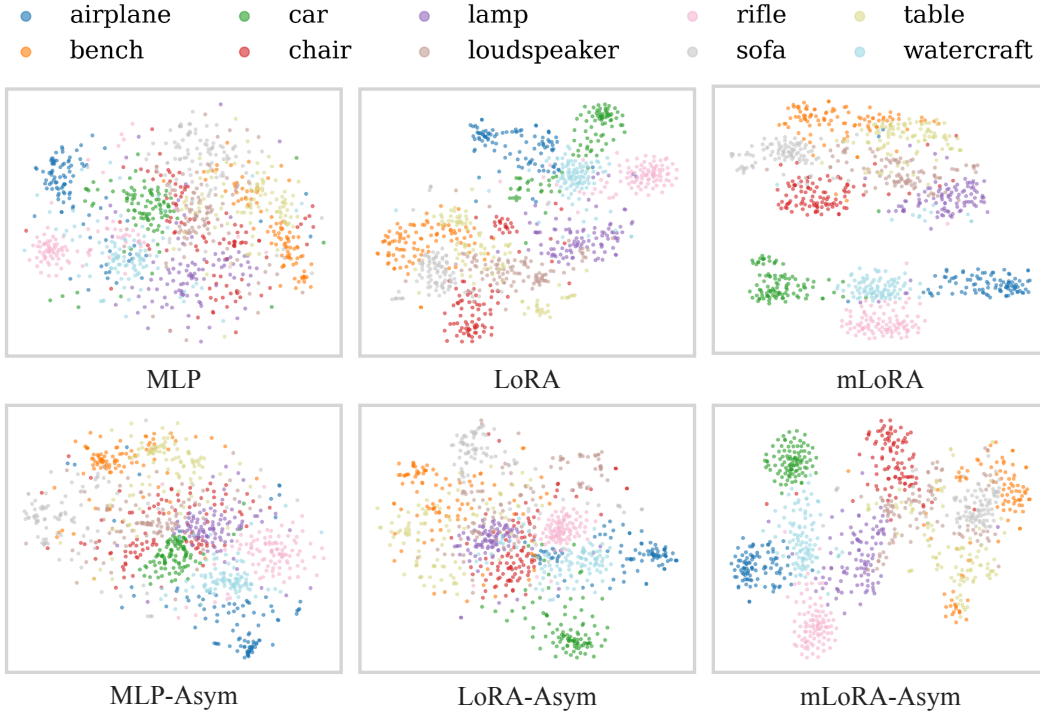


Figure 5: **t-SNE visualization of weight spaces.** Each point represents one instance from the ShapeNet ten-category dataset, colored by object category. Multiplicative LoRA weight spaces exhibit semantic structure.

First, our approach requires finetuning a base-model which is computationally more expensive than fitting small MLPs. This requirement prevents evaluation on datasets with hundreds of thousands of samples, constraining our experiments to datasets with thousands of instances. Future work could explore methods to eliminate this requirement, or develop more computationally efficient multiplicative LoRA adaptation procedures.

Second, we apply uniform parameter budgets across all layers in the neural field, treating each layer identically in terms of LoRA rank and capacity. However, different layers likely encode different levels of semantic abstraction, suggesting that adaptive parameter allocation could improve efficiency and representation quality.

Third, while our method achieves the first successful weight space generation on relatively high resolution natural images and demonstrates superior performance compared to prior weight space methods, the generation quality does not yet match state-of-the-art image generative models such as latent diffusion models. Future work could focus on closing this performance gap while preserving data modality agnosticism.

## 6 CONCLUSION

We have demonstrated that neural network weights can serve as effective data representations when constrained through appropriate inductive biases. By adapting a pre-trained base model via multiplicative LoRA, we transform the chaotic parameter space into structured weight representations that exhibit semantic organization, enabling superior reconstruction quality, generation performance, and semantic structure. Remarkably, mLoRA-Asym weights converge to a linear mode during optimization, and this structured weight space geometry correlates strongly with generative performance in diffusion models. These findings challenge the view of weights as opaque byproducts of optimization and establish their viability as semantic representations for reconstruction, generation, and discriminative tasks.



## Appendix

### 7 PERMUTATION SYMMETRY IN LoRA

We provide a formal proof that permutation symmetry exists within both additive and multiplicative LoRA parameterizations.

#### 7.1 PERMUTATION SYMMETRY IN ADDITIVE LoRA

**Theorem 1.** *The adapted weight matrix from additive LoRA exhibits permutation symmetry with respect to the rank dimensions.*

*Proof.* Consider the additive LoRA formulation:

$$\mathbf{W}' = \mathbf{W} + \mathbf{B}\mathbf{A} \quad (7)$$

where  $\mathbf{W} \in \mathbb{R}^{d_{\text{out}} \times d_{\text{in}}}$ ,  $\mathbf{A} \in \mathbb{R}^{r \times d_{\text{in}}}$ , and  $\mathbf{B} \in \mathbb{R}^{d_{\text{out}} \times r}$ .

From a neural network perspective, the operation  $\mathbf{B}\mathbf{A}\mathbf{x}$  for input  $\mathbf{x} \in \mathbb{R}^{d_{\text{in}}}$  can be viewed as a two layer network:

$$\mathbf{B}\mathbf{A}\mathbf{x} = \mathbf{B}(\mathbf{A}\mathbf{x}) \quad (8)$$

where  $\mathbf{A}$  acts as an encoder layer compressing the input to  $r$  hidden activations, and  $\mathbf{B}$  acts as a decoder layer expanding back to the output dimension.

Let  $\mathbf{h} = \mathbf{A}\mathbf{x} \in \mathbb{R}^r$  denote the hidden activations. Consider a permutation matrix  $\mathbf{P} \in \mathbb{R}^{r \times r}$  corresponding to permutation  $\pi$ . We can insert  $\mathbf{P}^T\mathbf{P} = \mathbf{I}$  between the two layers:

$$\mathbf{B}\mathbf{A}\mathbf{x} = \mathbf{B}\mathbf{P}^T\mathbf{P}\mathbf{A}\mathbf{x} = (\mathbf{B}\mathbf{P}^T)(\mathbf{P}\mathbf{A})\mathbf{x} \quad (9)$$

Define  $\tilde{\mathbf{A}} = \mathbf{P}\mathbf{A}$  and  $\tilde{\mathbf{B}} = \mathbf{B}\mathbf{P}^T$ . Then:

$$\mathbf{B}\mathbf{A} = \tilde{\mathbf{B}}\tilde{\mathbf{A}} \quad (10)$$

This shows that  $(\mathbf{B}, \mathbf{A})$  and  $(\tilde{\mathbf{B}}, \tilde{\mathbf{A}})$  produce identical adapted weight matrices. Concretely,  $\tilde{\mathbf{A}}$  permutes the rows of  $\mathbf{A}$  (equivalently, permutes which hidden neuron each row corresponds to), and  $\tilde{\mathbf{B}}$  permutes the columns of  $\mathbf{B}$  by the same permutation (matching the hidden neuron reordering).

Since there are  $r!$  possible permutations of  $r$  hidden neurons, and each permutation produces a functionally identical network, the additive LoRA weight space exhibits  $r!$ -fold permutation symmetry.  $\square$

*Remark 1.* This permutation symmetry is analogous to the well known permutation symmetry in standard MLPs Zhou et al. (2023a): reordering hidden neurons (along with their corresponding incoming and outgoing weights) does not change the function computed by the network. In LoRA, the hidden dimension is the rank  $r$ , and permuting this dimension induces the symmetry. Figure 6(a) illustrates this symmetry, showing how the low rank matrices can be viewed as encoder and decoder layers where intermediate neurons can be reordered.

#### 7.2 PERMUTATION SYMMETRY IN MULTIPLICATIVE LoRA

**Theorem 2.** *The adapted weight matrix from multiplicative LoRA can be expressed as a sum of base weight matrices, each pre-multiplied and post-multiplied by diagonal matrices.*

*Proof.* Consider the multiplicative LoRA formulation from Section 3.2:

$$\mathbf{W}' = \mathbf{W} \odot \mathbf{B}\mathbf{A} \quad (11)$$

where  $\mathbf{W} \in \mathbb{R}^{d_{\text{out}} \times d_{\text{in}}}$  is the base weight matrix,  $\mathbf{A} \in \mathbb{R}^{r \times d_{\text{in}}}$ , and  $\mathbf{B} \in \mathbb{R}^{d_{\text{out}} \times r}$ .

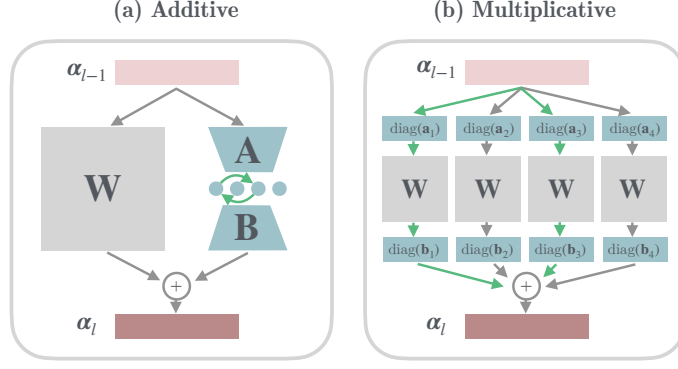


Figure 6: **Illustrating permutation symmetries within LoRA.** (a) Permutation symmetry in **additive** LoRA. Low rank matrices **A** and **B** could be seen as an encoder layer and a decoder layer. The order of the intermediate neurons could be swapped without changing the output. (b) **multiplicative** LoRA could be seen as parallel pathways with different scaling factors for the input and output. The order of the pathways could be swapped without changing the output.

We can decompose **B** and **A** into their column and row vectors respectively:

$$\mathbf{B} = [\mathbf{b}_1 \quad \mathbf{b}_2 \quad \cdots \quad \mathbf{b}_r], \quad \mathbf{A} = \begin{bmatrix} \mathbf{a}_1^T \\ \mathbf{a}_2^T \\ \vdots \\ \mathbf{a}_r^T \end{bmatrix} \quad (12)$$

where  $\mathbf{b}_i \in \mathbb{R}^{d_{\text{out}}}$  and  $\mathbf{a}_i \in \mathbb{R}^{d_{\text{in}}}$ .

Therefore:

$$\mathbf{W}' = \mathbf{W} \odot \left( \sum_{i=1}^r \mathbf{b}_i \mathbf{a}_i^T \right) = \sum_{i=1}^r \mathbf{W} \odot (\mathbf{b}_i \mathbf{a}_i^T) \quad (13)$$

For each term in the sum, the elementwise product  $\mathbf{W} \odot (\mathbf{b}_i \mathbf{a}_i^T)$  can be expressed using diagonal matrices. Let  $\text{diag}(\mathbf{b}_i)$  denote the diagonal matrix with  $\mathbf{b}_i$  on the diagonal, and similarly for  $\text{diag}(\mathbf{a}_i)$ . Then:

$$\mathbf{W} \odot (\mathbf{b}_i \mathbf{a}_i^T) = \text{diag}(\mathbf{b}_i) \mathbf{W} \text{diag}(\mathbf{a}_i) \quad (14)$$

This can be verified by examining the  $(j, k)$  entry:

$$[\mathbf{W} \odot (\mathbf{b}_i \mathbf{a}_i^T)]_{jk} = W_{jk} \cdot (b_i)_j \cdot (a_i)_k \quad (15)$$

$$= (b_i)_j \cdot W_{jk} \cdot (a_i)_k \quad (16)$$

$$= [\text{diag}(\mathbf{b}_i) \mathbf{W} \text{diag}(\mathbf{a}_i)]_{jk} \quad (17)$$

Therefore:

$$\mathbf{W}' = \sum_{i=1}^r \text{diag}(\mathbf{b}_i) \mathbf{W} \text{diag}(\mathbf{a}_i) \quad (18)$$

This shows that the adapted weight matrix is a sum of terms, where each term is the base weight matrix pre-multiplied and post-multiplied by diagonal matrices constructed from the LoRA parameters.  $\square$

**Corollary 2.1.** *Permuting the rank indices  $\{1, 2, \dots, r\}$  with a permutation  $\pi$  does not change the adapted weight matrix  $\mathbf{W}'$ , as summation is commutative. This implies permutation symmetry in the LoRA weight space.*

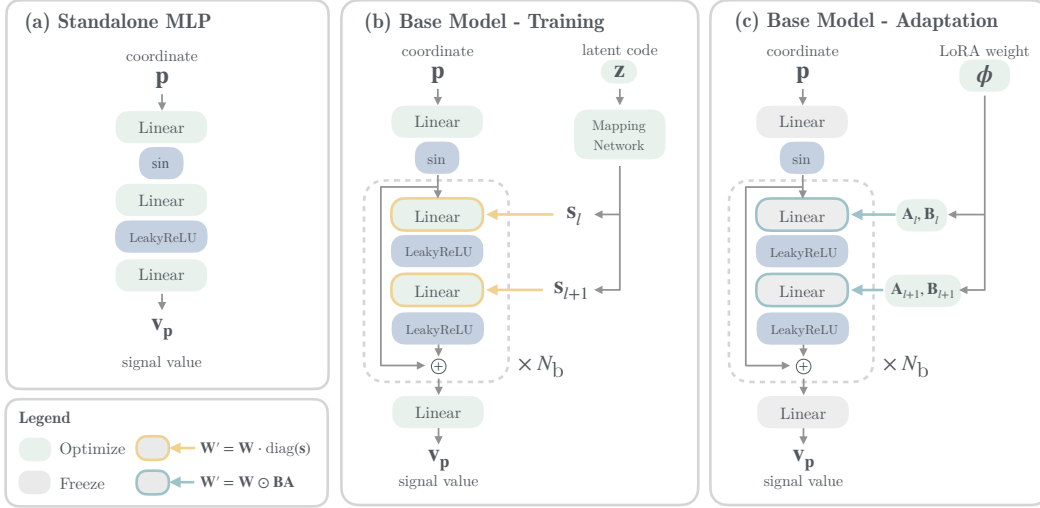


Figure 7: **Network architectures for weight space representations.** (a) Standalone MLP architecture with Fourier Feature layer followed by two linear layers. (b) Base model architecture with modulated fully connected layers. The network takes spatial coordinates  $\mathbf{p}$  and style vector  $\mathbf{s}$  as inputs, applying multiplicative weight modulation at each layer. (c) LoRA adaptation applied to the base model, where low rank matrices  $\mathbf{A}$  and  $\mathbf{B}$  adapt the frozen base weights.

This symmetry means that different configurations of LoRA parameters  $\{\mathbf{a}_i, \mathbf{b}_i\}_{i=1}^r$  can represent the same function, making the weight space representation ambiguous without additional constraints. Figure 6(b) visualizes this symmetry by showing how multiplicative LoRA can be interpreted as parallel pathways that can be reordered without affecting the output.

**Corollary 2.2.** *Once permutation symmetry is eliminated, multiplicative LoRA weights are aligned with the channels in the base network, i.e. each element corresponds to a single feature channel.*

*Proof.* In Equation 18, each term  $\text{diag}(\mathbf{b}_i)\mathbf{W}\text{diag}(\mathbf{a}_i)$  applies channel wise modulation to the base weight matrix  $\mathbf{W}$ . Specifically,  $\text{diag}(\mathbf{a}_i)$  scales the input channels, while  $\text{diag}(\mathbf{b}_i)$  scales the output channels. This operation preserves the channel structure of  $\mathbf{W}$  through element wise scaling rather than mixing features across channels. When permutation symmetry is eliminated through techniques such as asymmetric masking, each rank component  $i$  is uniquely identified and cannot be arbitrarily reordered. In this regime, each pair  $(\mathbf{a}_i, \mathbf{b}_i)$  corresponds to a specific modulation pattern applied to the base network channels.  $\square$

## 8 IMPLEMENTATION DETAILS

### 8.1 STANDALONE MLP

As shown in Figure 7(a), The standalone MLP is a Fourier Feature Tancik et al. (2020) layer  $\alpha_1 = \sin(\omega_0 \cdot (\mathbf{W}_1\mathbf{p} + \mathbf{b}_1))$  followed by 2 linear layers.

- $\omega_0$  is the frequency scaling factor for the Fourier Feature layer. For 2D FFHQ, we set  $\omega_0 = 32$ ; For 3D ShapeNet, we set  $\omega_0 = 1$ . This value is chosen empiracally and shared with its LoRA-based counterparts.
- $N_{\text{hidden}}$  is the number of hidden features in the linear layers. For the 2D FFHQ model, we use  $N_{\text{hidden}} = 94$  for all layers; For the 3D ShapeNet, we use  $N_{\text{hidden}} = 99$  for all layers, in order to have approximately the same number of learnable parameters as their LoRA-based counterparts.

As noted by Erkoç *et al.* Erkoç et al. (2023), an initialization trick is employed to ensure diffusion model generalization. Specifically, an MLP with weights  $\phi_0$  is fitted to one instance from the dataset, and used as a shared initialization for all the rest of the fittings  $\boldsymbol{\iota}_i = \phi_0$ . In other words, other instances are fitted by fine-tuning the weights from the first instance. This trick is crucial to the performance of HyperDiffusion, and therefore we employ it in the FFHQ and ShapeNet airplane experiments. However, in the multi-category experiment, it does not make sense to initialize a *chair* fitting with weights from an *airplane*, therefore we do not use this trick and instead use a shared random initialization for all the fittings, like is done for the LoRA-based weight representations.

For each instance, we run 10k steps, each step with 8,192 points with an Adam optimizer, where learning rate adaptively decay from  $10^{-2}$  to  $10^{-5}$ . The same optimizer and hyperparameters are used for the LoRA-based weight representations.

## 8.2 BASE MODEL ARCHITECTURE

The base model follows the modulated neural field architecture widely adopted in generative neural field works Anokhin et al. (2021); Karras et al. (2021); Chan et al. (2020), as illustrated in Figure 7(b). The architecture consists of a mapping network and a synthesis network. The mapping network is a multilayer perceptron that transforms a latent code  $\mathbf{z} \in \mathbb{R}^{d_z}$  into intermediate style vectors  $\{\mathbf{s}_l\}_{l=1}^L$ , where  $L$  is the number of synthesis layers. For 2D FFHQ, we use  $d_z = 256$  and an 8 layer mapping network with hidden dimension 256. For 3D ShapeNet, we use  $d_z = 128$  and a 4 layer mapping network with hidden dimension 256.

The synthesis network takes spatial coordinates  $\mathbf{p}$  as input and produces signal values through a sequence of synthesis blocks, each block contains 2 modulated fully connected. The blocks are connected with residual connections to ensure gradient flow. Each layer  $l$  first applies weight modulation, where the weight matrix  $\mathbf{W}_l$  is scaled by a learned affine transformation of the style vector:  $\mathbf{W}'_l = \mathbf{W}_l \cdot \text{diag}(\mathbf{s}_l)$ , where  $\mathbf{s}_l = \mathbf{A}_l \mathbf{s} + \mathbf{b}_l$  is computed from the style vector via an affine transformation. The modulated weights are then normalized per output channel as  $w'_{ijk} = w'_{ijk} / \sqrt{\sum_{i,k} (w'_{ijk})^2 + \epsilon}$ , where  $\epsilon = 10^{-8}$  for numerical stability. The layer then computes activations as  $\boldsymbol{\alpha}_{l+1} = \text{ReLU}(\mathbf{W}'_l \boldsymbol{\alpha}_l + \mathbf{b}_l)$ . For 2D FFHQ, we use 6 synthesis blocks with channel dimensions 256. For 3D ShapeNet, we use 4 synthesis blocks with channel dimensions 512.

## 8.3 BASE MODEL TRAINING

We devise a multistage progressive training strategy that gradually increases sampling resolution while decreasing batch size. Early stages use large batch sizes with low resolution (batch size of 256 with 2,048 points per instance) to establish the latent code manifold, while late stages use small batch sizes with high resolution (batch size of 16 with 32,768 points per instance) to capture fine details. This strategy ensures stable latent code initialization while maintaining computational efficiency.

We train 350k steps with an Adam optimizer, where the learning rate gradually decay from  $10^{-3}$  to  $10^{-5}$  in 5 stages. For regularization factor we use  $\lambda_r = 10^{-4}$ . Exponential moving average is applied on the base model weights.

## 8.4 DATASET

For FFHQ, we use the first 5,000 samples from the dataset for all our experiments. For ShapeNet airplane, we use all 4,045 samples. To create the ShapeNet 10-category dataset, we select the top 10 categories with the most samples and then randomly sample 500 instances from each category.

**Algorithm 1** Pipeline for weight space learning and generation.

---

```

1: Input: Dataset  $\{\mathbf{x}_i\}_{i=1}^N$ , parameterization type  $\tau \in \{\text{MLP}, \text{LoRA}, \text{mLoRA}\}$ 
2: Output: Trained diffusion model  $\epsilon_\theta$ 

3: Stage 1: Base Model Training (for LoRA/mLoRA only)
4: if  $\tau \in \{\text{LoRA}, \text{mLoRA}\}$  then
5:   Initialize base model weights  $\theta$  and latent codes  $\{\mathbf{z}_i\}_{i=1}^N$ 
6:   Jointly optimize  $\theta$  and  $\{\mathbf{z}_i\}$  via variational autodecoding:
7:    $\theta^*, \{\mathbf{z}_i^*\} \leftarrow \arg \min_{\theta, \{\mathbf{z}_i\}} \sum_{i=1}^N \mathcal{L}_{\text{recon}}(f(\mathbf{p}, \mathbf{z}_i | \theta), \mathbf{x}_i(\mathbf{p})) + \lambda_r \|\mathbf{z}_i\|_2^2$ 
8:   Freeze base model:  $\theta \leftarrow \theta^*$ 
9: end if

10: Stage 2: Instance Fitting
11: if  $\tau = \text{MLP}$  then
12:   Fit one instance:
13:    $\phi_0 \leftarrow \arg \min_{\phi} \mathcal{L}_{\text{recon}}(f(\mathbf{p} | \phi), \mathbf{x}_1(\mathbf{p}))$ 
14:   for  $i = 2$  to  $N$  do
15:     Initialize:  $\phi_i \leftarrow \phi_0$ 
16:     Optimize:
17:      $\phi_i \leftarrow \arg \min_{\phi} \mathcal{L}_{\text{recon}}(f(\mathbf{p} | \phi), \mathbf{x}_i(\mathbf{p}))$ 
18:   end for
19: else
20:   Sample shared random initialization:  $\iota_0 \sim \mathcal{N}(0, \mathbf{I})$ 
21:   for  $i = 1$  to  $N$  do
22:     Initialize:  $\phi_i \leftarrow \iota_0$ 
23:     Optimize:
24:      $\phi_i \leftarrow \arg \min_{\phi} \mathcal{L}_{\text{recon}}(f(\mathbf{p} | \text{LoRA}(\mathbf{W}, \phi)), \mathbf{x}_i(\mathbf{p}))$ 
25:   end for
26: end if

27: Stage 3: Diffusion Model Training
28: Initialize diffusion model parameters  $\nu$ 
29: while not converged do
30:   Sample  $t \sim \mathcal{U}(1, T)$ ,  $\phi_0 \sim \{\phi_i\}_{i=1}^N$ ,  $\epsilon \sim \mathcal{N}(0, \mathbf{I})$ 
31:   Compute  $\phi_t = \sqrt{\alpha_t} \phi_0 + \sqrt{1 - \alpha_t} \epsilon$ 
32:   Update:  $\nu \leftarrow \nu - \nabla_{\nu} \|\epsilon - \epsilon_{\nu}(\phi_t, t)\|^2$ 
33: end while
34: return  $\epsilon_\theta$ 

```

---

## 8.5 PIPELINE

Algorithm 1 describes the complete pipeline for weight space representation learning and generation. The process consists of three stages: First, we train a base model using variational autodecoding for LoRA based representations. Second, we construct a dataset of weight representations by fitting neural fields to individual instances. For standalone MLP, an initialization trick is employed where one instance is first fitted and then used to initialize all other fittings. For LoRA based representations, all instances share the same random initialization. Third, we train a diffusion model on the collected weight representations to enable generation of novel instances.

For the diffusion model architecture, we use a standard Diffusion Transformer (DiT) Peebles & Xie (2022) for standalone MLP weights. For LoRA weights, we employ the hierarchical LoRA layer encoder described in Section 3.5 of the main paper. During training, we use the DDPM objective with a linear noise schedule from  $\beta_1 = 10^{-4}$  to  $\beta_T = 2 \times 10^{-2}$  over  $T = 500$  timesteps. For generation, we use DDIM sampling with 100 steps to efficiently sample new weight representations. The diffusion transformer has 2880 hidden size (i.e., the size of each token after linear projection or layer encoder), 12 layers, and 16 self-attention heads. We

train the diffusion transformer with batch size of 256 and learning rate of  $2 \times 10^{-4}$  for 6000 epochs until convergence.

## 9 EVALUATION METRICS FOR GENERATION

We calculate distributional metrics for both 2D and 3D. For 3D, we also calculate distance-based metrics. All metrics are calculated between 2,048 generated samples and 2,048 reference samples.

### 9.1 DISTRIBUTIONAL DIFFERENCE

These metrics operate on features extracted by deep learned models, as deep learned feature extractors project the data into semantically rich embedding spaces where distances better correlate with human perception of similarity. We employ these metrics in their mathematical form rather than using modality-specific implementations like FID Heusel et al. (2017) or KID Bińkowski et al. (2018), as this allows for consistent evaluation across different data modalities. For 2D images, we use CLIP Radford et al. (2021) as the feature extractor; for 3D shapes, we use a PointNet++ Qi et al. (2017).

Given generated distribution  $P$  and reference distribution  $Q$ , to make the metric more comparable, we first normalize the extracted features by

$$\boldsymbol{\rho} \leftarrow \frac{\boldsymbol{\rho} - \mu_Q}{\sigma_Q}$$

for both the generated set and reference set, where  $\mu_Q$  and  $\sigma_Q$  are the scalar mean and standard deviation calculated from the reference set.

**Fréchet Distance (FD)** Fréchet (1957) measures the distance between two multivariate Gaussian distributions fitted to feature representations of generated and reference samples. Given feature representations from a pretrained network, we compute the mean  $\boldsymbol{\mu}_P$  and covariance  $\boldsymbol{\Sigma}_P$  for generated distribution  $P$  and mean  $\boldsymbol{\mu}_Q$  and covariance  $\boldsymbol{\Sigma}_Q$  for reference distribution  $Q$ . The Fréchet Distance is then computed as:

$$\text{FD}(P, Q) = \frac{1}{N_{\text{feature}}} [\|\boldsymbol{\mu}_P - \boldsymbol{\mu}_Q\|_2^2 + \text{Tr}(\boldsymbol{\Sigma}_P + \boldsymbol{\Sigma}_Q - 2(\boldsymbol{\Sigma}_P \boldsymbol{\Sigma}_Q)^{1/2})].$$

where  $N_{\text{feature}}$  is the feature dimension of the feature extractor.

**Maximum Mean Discrepancy (MMD)** with respect to a positive definite kernel  $\psi$  is defined by:

$$\text{MMD}(P, Q) = \mathbb{E}_{\mathbf{x}, \mathbf{x}'}[\psi(\mathbf{x}, \mathbf{x}')] + \mathbb{E}_{\mathbf{y}, \mathbf{y}'}[\psi(\mathbf{y}, \mathbf{y}')] - 2\mathbb{E}_{\mathbf{x}, \mathbf{y}}[\psi(\mathbf{x}, \mathbf{y})],$$

where  $\mathbf{x}, \mathbf{x}' \sim P$  are samples from the generated distribution and  $\mathbf{y}, \mathbf{y}' \sim Q$  are samples from the reference distribution. This metric does not make the multivariate Gaussian assumption and is reported to be more reliable and sample efficient Jayasumana et al. (2024); Bińkowski et al. (2018). We calculate this metric with 2 types of kernels.

1. Polynomial kernel (MMD-P)  
 $\psi_p(\mathbf{x}, \mathbf{y}) = (\gamma_p \cdot \mathbf{x}^T \mathbf{y} + c)^d$  with degree  $d = 3$  and offset  $c = 1$ . Following the practice of KID Bińkowski et al. (2018), we choose  $\gamma_p = 1/N_{\text{feature}}$ .
2. Gaussian RBF kernel (MMD-G)  
 $\psi_g(\mathbf{x}, \mathbf{y}) = \exp(-\gamma_g \|\mathbf{x} - \mathbf{y}\|_2^2)$  with  $\gamma_g = 1/(2\sigma_g^2)$ ; we choose  $\sigma_g = N_{\text{feature}}$ .

### 9.2 DISTANCE-BASED METRICS FOR 3D SHAPES

For 3D shapes, we calculate distance-based metrics following Erkoç et al. (2023); Vahdat et al. (2022); Luo & Hu (2021); Zhou et al. (2021). We denote the distance function as

Table 5: Ablation study of LoRA Layer Encoder on 3D ShapeNet - 10 category.

	ShapeNet - Multi					
	mMD ↓	COV ↑	1-NNA ↓	FD ↓	MMD-G ↓	MMD-P ↓
w/o	<b>5.18</b>	47.7%	61.2%	0.049	0.008	0.098
with	5.52	<b>49.6%</b>	<b>58.6%</b>	<b>0.026</b>	<b>0.004</b>	<b>0.040</b>

$D(\mathbf{x}, \mathbf{y})$  for the Chamfer Distance between two shapes  $\mathbf{x}$  and  $\mathbf{y}$ . The metrics are defined as:

$$\begin{aligned} \text{mMD}(P, Q) &= \mathbb{E}_{\mathbf{y} \sim Q} \left[ \min_{\mathbf{x} \sim P} D(\mathbf{x}, \mathbf{y}) \right], \\ \text{COV}(P, Q) &= \frac{|\{\arg \min_{\mathbf{y} \sim Q} D(\mathbf{x}, \mathbf{y}) | \mathbf{x} \sim P\}|}{|Q|}, \\ \text{1-NNA}(P, Q) &= \frac{\sum_{\mathbf{x} \sim P} \mathbb{1}[\mathbf{N}_{\mathbf{x}} \sim P] + \sum_{\mathbf{y} \sim Q} \mathbb{1}[\mathbf{N}_{\mathbf{y}} \sim Q]}{|P| + |Q|}, \end{aligned}$$

where in the 1-NNA metric  $\mathbf{N}_{\mathbf{x}}$  is the shape that is closest to  $\mathbf{x}$  in both generated and reference distributions, that is,

$$\mathbf{N}_{\mathbf{x}} = \arg \min_{\mathbf{z} \sim P \cup Q} D(\mathbf{x}, \mathbf{z}).$$

For mMD, lower is better; for COV, higher is better; for 1-NNA, 50% is optimal.

## 10 ABLATION STUDY

We examine the effectiveness of the hierarchical LoRA layer encoder introduced in Section 3.5. To isolate its contribution, we train a baseline diffusion model without the layer encoder on the ShapeNet multi-category dataset. This baseline treats each weight matrix as an independent token, directly feeding flattened LoRA matrices into the transformer without the hierarchical processing that models within layer rank dependencies and cross layer relationships.

Table 5 compares the baseline against our full model with the hierarchical layer encoder. The results demonstrate that the layer encoder provides substantial improvements across all metrics. The full model achieves higher coverage (49.6% vs 47.7%), better 1-NNA (58.6% vs 61.2%), and significantly better distributional metrics: FD improves from 0.049 to 0.026, MMD-G from 0.008 to 0.004, and MMD-P from 0.098 to 0.040. These improvements confirm that explicitly modeling the compositional structure of LoRA weights, where rank components within each layer interact and different layers encode different semantic levels, is essential for effective weight space generation. The hierarchical design enables the diffusion model to respect the intrinsic organization of neural field weights, leading to higher quality generated samples.

## 11 ADDITIONAL QUALITATIVE RESULTS ON GENERATION

We provide additional qualitative results on diffusion generation. Please see Figure 8 for results on ShapeNet Airplanes, Figure 9 for results on ShapeNet Multi, and Figure 10 for results on FFHQ.

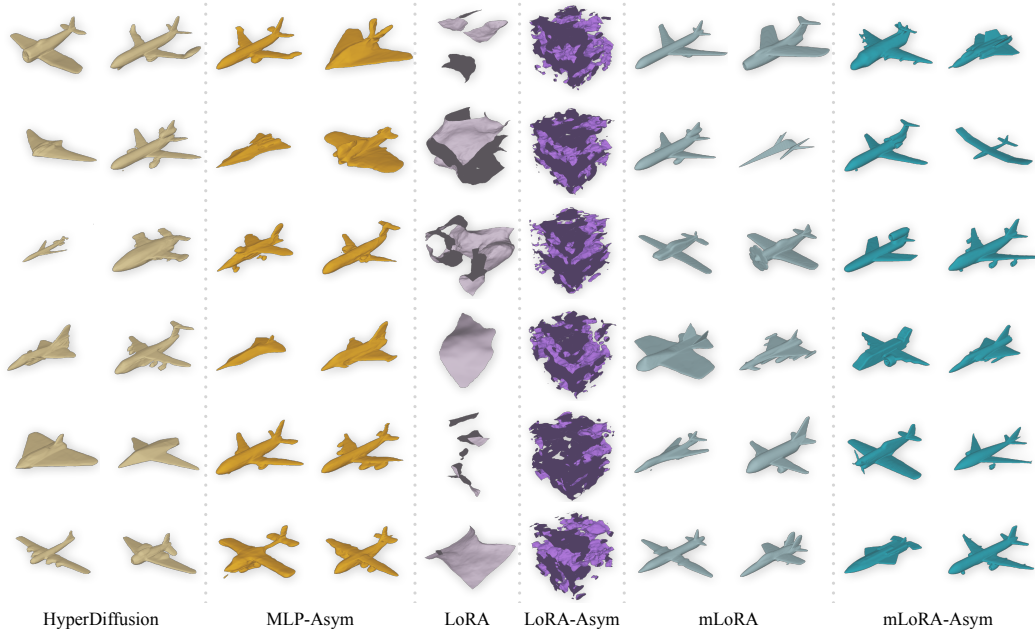


Figure 8: **Additional qualitative generation results on ShapeNet - Airplanes.**

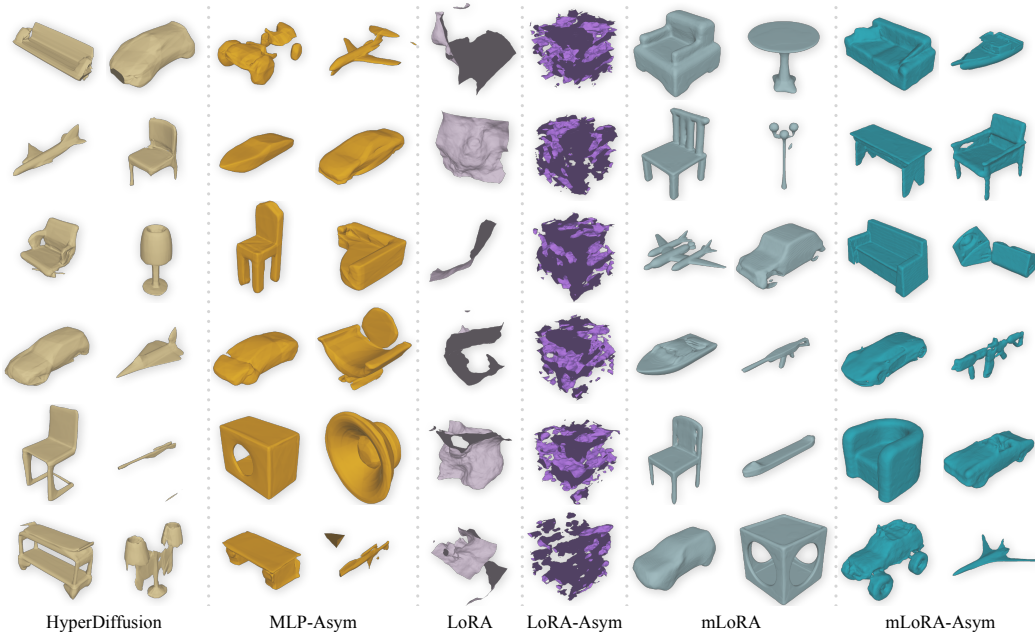


Figure 9: **Additional qualitative generation results on ShapeNet - Multi.**



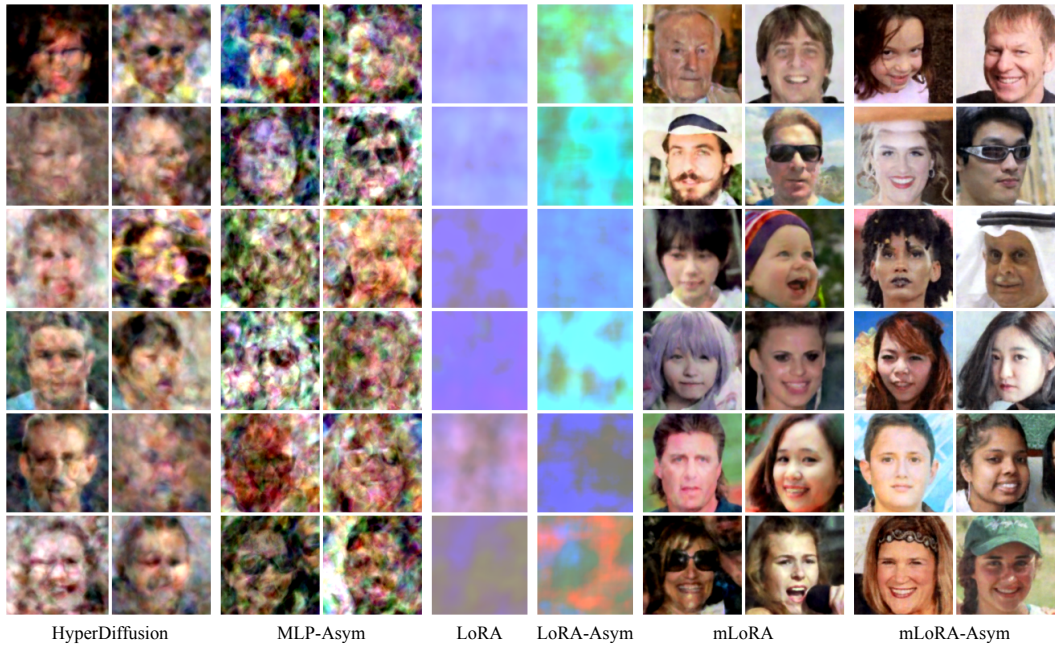


Figure 10: **Additional qualitative generation results on FFHQ.**

## REFERENCES

- Ivan Anokhin, Kirill Demochkin, Taras Khakhulin, Gleb Sterkin, Victor Lempitsky, and Denis Korzhenkov. Image generators with conditionally-independent pixel synthesis. In *Proceedings of the IEEE/CVF conference on computer vision and pattern recognition*, pp. 14278–14287, 2021.
- Mikołaj Bińkowski, Danica J Sutherland, Michael Arbel, and Arthur Gretton. Demystifying mmd gans. *arXiv preprint arXiv:1801.01401*, 2018.
- Eric R Chan, Marco Monteiro, Petr Kellnhofer, Jiajun Wu, and Gordon Wetzstein. pi-gan: Periodic implicit generative adversarial networks for 3d-aware image synthesis. arxiv e-prints, page. *arXiv preprint arXiv:2012.00926*, 2020.
- Angel X Chang, Thomas Funkhouser, Leonidas Guibas, Pat Hanrahan, Qixing Huang, Zimo Li, Silvio Savarese, Manolis Savva, Shuran Song, Hao Su, et al. Shapenet: An information-rich 3d model repository. *arXiv preprint arXiv:1512.03012*, 2015.
- Yinbo Chen and Xiaolong Wang. Transformers as meta-learners for implicit neural representations. In *European Conference on Computer Vision*, pp. 170–187. Springer, 2022.
- Amil Dravid, Yossi Gandelsman, Kuan-Chieh Wang, Rameen Abdal, Gordon Wetzstein, Alexei Efros, and Kfir Aberman. Interpreting the weight space of customized diffusion models. *Advances in Neural Information Processing Systems*, 37:137334–137371, 2024.
- Emilien Dupont, Adam Goliński, Milad Alizadeh, Yee Whye Teh, and Arnaud Doucet. Coin: Compression with implicit neural representations. *arXiv preprint arXiv:2103.03123*, 2021.
- Ziya Erkoç, Fangchang Ma, Cengiz Öztireli, and Pascal Fua. Hyperdiffusion: Generating implicit neural fields with weight-space diffusion. In *International Conference on Computer Vision*, 2023.
- Amer Essakine, Yanqi Cheng, Chun-Wun Cheng, Lipei Zhang, Zhongying Deng, Lei Zhu, Carola-Bibiane Schönlieb, and Angelica I Aviles-Rivero. Where do we stand with implicit neural representations? a technical and performance survey. *arXiv preprint arXiv:2411.03688*, 2024.
- Jonathan Frankle, Gintare Karolina Dziugaite, Daniel Roy, and Michael Carbin. Linear mode connectivity and the lottery ticket hypothesis. In *International Conference on Machine Learning*, pp. 3259–3269. PMLR, 2020.
- Maurice Fréchet. Sur la distance de deux lois de probabilité. In *Annales de l’ISUP*, volume 6, pp. 183–198, 1957.
- Y Gao and Others. Revisiting model merging: A statistical perspective. *arXiv preprint*, 2024.
- Cameron Gordon, Lachlan E MacDonald, Hemanth Saratchandran, and Simon Lucey. D’oh: Decoder-only random hypernetworks for implicit neural representations. In *Proceedings of the Asian Conference on Computer Vision*, pp. 2507–2526, 2024.
- David Ha, Andrew Dai, and Quoc V Le. Hypernetworks. In *International Conference on Learning Representations*, 2016.
- Martin Heusel, Hubert Ramsauer, Thomas Unterthiner, Bernhard Nessler, and Sepp Hochreiter. Gans trained by a two time-scale update rule converge to a local nash equilibrium. *Advances in neural information processing systems*, 30, 2017.
- T Hospedales, A Antoniou, P Micaelli, and A Storkey. Meta-learning in neural networks: a survey. arxiv preprint arxiv: 200405439. 2020.
- Edward J Hu, Yelong Shen, Phillip Wallis, Zeyuan Allen-Zhu, Yuanzhi Li, Shean Wang, Lu Wang, Weizhu Chen, et al. Lora: Low-rank adaptation of large language models. *ICLR*, 1(2):3, 2022.

- Sadeep Jayasumana, Srikumar Ramalingam, Andreas Veit, Daniel Glasner, Ayan Chakrabarti, and Sanjiv Kumar. Rethinking fid: Towards a better evaluation metric for image generation. In *Proceedings of the IEEE/CVF Conference on Computer Vision and Pattern Recognition*, pp. 9307–9315, 2024.
- Tero Karras, Samuli Laine, and Timo Aila. A style-based generator architecture for generative adversarial networks. In *Proceedings of the IEEE/CVF conference on computer vision and pattern recognition*, pp. 4401–4410, 2019.
- Tero Karras, Miika Aittala, Samuli Laine, Erik Härkönen, Janne Hellsten, Jaakko Lehtinen, and Timo Aila. Alias-free generative adversarial networks. *Advances in neural information processing systems*, 34:852–863, 2021.
- Sylwester Kloczek, Lukasz Maziarka, Maciej Wołczyk, Jacek Tabor, Jakub Nowak, and Marek Śmieja. Hypernetwork functional image representation. In *International Conference on Artificial Neural Networks*, pp. 496–510. Springer, 2019.
- M Kofinas, B Knyazev, Y Zhang, Y Chen, G J Burghouts, E Gavves, C G M Snoek, and D W Zhang. Graph neural networks for learning equivariant representations of neural networks. In *The Twelfth International Conference on Learning Representations*, 2024.
- D Lim, Y Gelberg, S Jegelka, H Maron, et al. Learning on lorax: Gl-equivariant processing of low-rank weight spaces for large finetuned models. *arXiv preprint arXiv:2410.04207*, 2024a.
- Derek Lim, Theo Putterman, Robin Walters, Haggai Maron, and Stefanie Jegelka. The empirical impact of neural parameter symmetries, or lack thereof. *Advances in Neural Information Processing Systems*, 37:28322–28358, 2024b.
- Shitong Luo and Wei Hu. Diffusion probabilistic models for 3d point cloud generation. In *Proceedings of the IEEE/CVF conference on computer vision and pattern recognition*, pp. 2837–2845, 2021.
- A Navon, A Shamsian, I Achituve, E Fetaya, G Chechik, and H Maron. Equivariant architectures for learning in deep weight spaces. In *International Conference on Machine Learning*, pp. 25790–25816, 2023.
- O Ormaniec and Others. Fusion of graph convolutional networks via optimal transport. *arXiv preprint*, 2025.
- Jeong Joon Park, Peter Florence, Julian Straub, Richard Newcombe, and Steven Lovegrove. DeepSDF: Learning continuous signed distance functions for shape representation. In *Proceedings of the IEEE/CVF conference on computer vision and pattern recognition*, pp. 165–174, 2019.
- William Peebles, Ilija Radosavovic, Tim Brooks, Alexei A Efros, and Jitendra Malik. Learning to learn with generative models of neural network checkpoints. *arXiv preprint arXiv:2209.12892*, 2023.
- William S Peebles and Saining Xie. Scalable diffusion models with transformers. 2023 IEEE. In *CVF International Conference on Computer Vision (ICCV)*, volume 4172, 2022.
- Charles Ruizhongtai Qi, Li Yi, Hao Su, and Leonidas J Guibas. Pointnet++: Deep hierarchical feature learning on point sets in a metric space. *Advances in neural information processing systems*, 30, 2017.
- Alec Radford, Jong Wook Kim, Chris Hallacy, Aditya Ramesh, Gabriel Goh, Sandhini Agarwal, Girish Sastry, Amanda Askell, Pamela Mishkin, Jack Clark, et al. Learning transferable visual models from natural language supervision. In *International conference on machine learning*, pp. 8748–8763. PmLR, 2021.
- C Singh and M Jaggi. Model fusion via optimal transport. In *Advances in Neural Information Processing Systems*, 2020.

- Jaisidh Singh, Diganta Misra, and Boris Knyazev. Hyper-align: Efficient modality alignment via hypernetworks. In *Workshop on Neural Network Weights as a New Data Modality*.
- Matthew Tancik, Pratul Srinivasan, Ben Mildenhall, Sara Fridovich-Keil, Nithin Raghavan, Utkarsh Singhal, Ravi Ramamoorthi, Jonathan Barron, and Ren Ng. Fourier features let networks learn high frequency functions in low dimensional domains. *Advances in neural information processing systems*, 33:7537–7547, 2020.
- Arash Vahdat, Francis Williams, Zan Gojcic, Or Litany, Sanja Fidler, Karsten Kreis, et al. Lion: Latent point diffusion models for 3d shape generation. *Advances in Neural Information Processing Systems*, 35:10021–10039, 2022.
- Kushal Vyas, Ahmed I Humayun, Aniket Dashpute, Richard G Baraniuk, Ashok Veeraghavan, and Guha Balakrishnan. Learning transferable features for implicit neural representations. *Advances in Neural Information Processing Systems*, 37:42268–42291, 2024.
- K Wang and Others. Scaling weight space generative models. *arXiv preprint*, 2025.
- K Wang, Z Xu, Y Zhou, Z Zang, T Darrell, Z Liu, and Y You. Neural network diffusion. *arXiv preprint arXiv:2402.13144*, 2024.
- Yiheng Xie, Towaki Takikawa, Shunsuke Saito, Or Litany, Shiqin Yan, Numair Khan, Federico Tombari, James Tompkin, Vincent Sitzmann, and Srinath Sridhar. Neural fields in visual computing and beyond. In *Computer graphics forum*, volume 41, pp. 641–676. Wiley Online Library, 2022.
- Enneng Yang, Li Shen, Guibing Guo, Xingwei Wang, Xiaochun Cao, Jie Zhang, and Dacheng Tao. Model merging in llms, mllms, and beyond: Methods, theories, applications and opportunities. *arXiv preprint arXiv:2408.07666*, 2024.
- Gizem Yüce, Guillermo Ortiz-Jiménez, Beril Besbinar, and Pascal Frossard. A structured dictionary perspective on implicit neural representations. In *Proceedings of the IEEE/CVF Conference on Computer Vision and Pattern Recognition*, pp. 19228–19238, 2022.
- Bo Zhao, Robin Walters, and Rose Yu. Symmetry in neural network parameter spaces. *arXiv preprint arXiv:2506.13018*, 2025.
- Allan Zhou, Kaien Yang, Kaylee Burns, Adriano Cardace, Yiding Jiang, Samuel Sokota, J Zico Kolter, and Chelsea Finn. Permutation equivariant neural functionals. *Advances in neural information processing systems*, 36:24966–24992, 2023a.
- Allan Zhou, Kaien Yang, Yiding Jiang, Kaylee Burns, Winnie Xu, Samuel Sokota, J Zico Kolter, and Chelsea Finn. Neural functional transformers. *Advances in neural information processing systems*, 36:77485–77502, 2023b.
- Linqi Zhou, Yilun Du, and Jiajun Wu. 3d shape generation and completion through point-voxel diffusion. In *Proceedings of the IEEE/CVF international conference on computer vision*, pp. 5826–5835, 2021.